INT. J. REMOTE SENSING, 20 DECEMBER, 2004,
VOL. 25, NO. 24, 5705–5729

Taylor & Francis
Taylor & Francis Group

Snow surface albedo estimation using terrestrial photography

J. G. CORRIPIO*

Department of Geography, University of Edinburgh, Drummond Street, Edinburgh EH8 9XP, UK

(*Received 24 July 2002; in final form 13 February 2004*)

Abstract. A flexible and inexpensive remote sensing tool for albedo estimation using conventional terrestrial photography and its validation on an Alpine glacier are described. The proposed technique involves georeferencing oblique photographs to a digital elevation model (DEM), defining a mapping function between the information contained on a given pixel of the image and the corresponding cell of the DEM. This is attained by performing a perspective projection of the DEM after a viewing transformation into the camera coordinate system. Once the image is georeferenced, the reflectance values recorded by the film or digital camera are corrected for topographic and atmospheric influences and for the effect of the photographic process (lens-film-developing-scanning). Atmospheric transmittance is evaluated using the MODTRAN radiative transfer model. Diffuse and direct irradiation are estimated using a parametric solar irradiation model. The solar-ground geometry, anisotropy of reflected radiation, the effect of surrounding topography and the portion of visible sky are evaluated using terrain algorithms applied to the DEM. The response of the camera-film-scanner system is evaluated using an empirical approach. The result is a geographically correct map of normalized reflectance values. By comparing these to a surface of known albedo, the spatial distribution of albedos is calculated. Comparisons to *in situ* measurements on the Mer de Glace glacier, French Alps, show good agreement. Sources of error are identified and ways of improvement addressed. The georeferencing algorithm, implemented into the Interactive Data Language (IDL) is available from the author and at the user contributed IDL library at www.rsinc.com.

1. Aim

The overall aim of this work is to develop a practical and inexpensive remote sensing tool for the estimation of temporal and spatial variations of surface albedo on glacier and snow-covered mountainous areas. Given that the maximum energy reflected by the snow lies on the visible band of the electromagnetic spectrum, and given the widespread use of photographic cameras, the good spectral response of modern films and the increasing availability of digital photography, the use of conventional photography was explored for this purpose.

*Now at: Institute of Hydromechanics and Water Resources Management, Swiss Federal Institute of Technology, ETH—Hönggerberg HIL G 28.1, CH-8093 Zürich, Switzerland; e-mail: Javier.Corripio@ethz.ch

International Journal of Remote Sensing
ISSN 0143-1161 print/ISSN 1366-5901 online © 2004 Taylor & Francis Ltd
http://www.tandf.co.uk/journals
DOI: 10.1080/01431160410001709002

2. Introduction

On low and mid-latitude glaciers and on high mountains, solar radiation is the main source of energy for the melting of ice and snow (e.g. de la Casinière 1974, Marks and Dozier 1992, Cline 1997). Thus an accurate measurement of the temporal and spatial variation of albedo, which is the ratio of incoming to outgoing hemispherical shortwave radiation, is necessary to estimate snow ablation, which consequently influences the glacier mass balance and the meltwater run-off. Albedo is, therefore, a very important parameter for the study of the hydrological resources derived from snow and for the study of glacier behaviour and its climatic response. It is an essential input for the physically based estimation of the energy balance of glaciers and snow cover basins (e.g. Strasser *et al*. 2002).

In order to estimate the albedo distribution over a basin, a standard approach is the interpolation of values from a few point measurements. However, the high spatial variability of albedo may introduce a large error (Knap *et al*. 1999). Furthermore, *in situ* measurements may be difficult or even impossible due to avalanche risk, making remote sensing tools an attractive solution. Satellite remote sensing has the potential to provide the necessary information on spatial and temporal variations of albedo, and therefore considerable research is being done in this area (e.g. Dubayah 1992, Knap *et al*. 1999, Grover *et al*. 2000). Although satellite-derived data are very cost-effective they may still become expensive, especially if a high temporal resolution is required. Additionally, in areas of high relief, cloud cover and shadows may reduce the efficiency of satellite imagery in the visible and infrared bands, and it is impossible to get a temporal resolution higher than the repeat coverage cycle of the satellite.

An economic and either alternative or complementary approach to satellite imagery is the use of oblique terrestrial photography, which allows high temporal and spatial resolution. Furthermore, the combination of both techniques, satellite and photography, may enhance the quality of the satellite data. By testing smaller sites at higher resolution the results can be validated for the the whole coverage area. The proposed technique is suitable for mountainous regions where views at a steep incidence angle yield a better precision for the georeferencing process and larger ground coverage. The technique was evaluated by using the Mer de Glace Glacier in the French Alps, as a test site.

3. Methodology

In this section the mathematical approach to defining the camera coordinate system is explained, together with the geometric transformations needed for georeferencing oblique photography. Visibility analysis is performed and basic photograph orientation and corrections for camera movements are considered. Problems arising from using non-metric cameras and conventional film and scanner are addressed. First we describe the georeferencing of oblique photographic images using a viewing transformation and perspective projection of a digital elevation model (DEM) and a mapping function between pixels in the photograph and cells in the DEM. Then we deal with the estimation of albedo from reflectance values recorded by the camera. This is done by obtaining the ratio between the reflectance normalized values of the georeferenced photograph and a surface of known albedo. The effect of topography on the global solar radiation arriving at the ground is studied, accounting for direct cast shadows, diffuse radiation from the sky and diffuse reflected radiation from the surrounding terrain, which can be important in snow-covered areas. The attenuation of solar radiation reflected from the target

pixels when traversing the intervening atmosphere is evaluated with the help of a radiative transfer model (MODTRAN) and a simple empirical relationship is found for the effect of the camera optics, scan and film developing on the final product and the digital reflectance values in the image of the studied area. Finally the preferred data storage format is justified.

3.1. *Georeferencing terrestrial photography*

In order to georeference terrestrial photographs we need to find a function relating two-dimensional pixels in the photograph to three-dimensional points in the DEM. This is achieved by applying a perspective projection after transforming the coordinates of the DEM to the camera coordinate system. In this way we produce a 'virtual' photograph of the DEM, that is, a twodimensional representation of the relief information contained in the DEM, as seen from the point of view of the camera. By scaling this representation according to the resolution of the photograph, we can establish the necessary correspondence between pixels in the image, screen coordinates of the perspective projection of the DEM and their geographic location.

Simultaneous development of a similar technique has been carried out by different authors (Corripio 2000, 2001, Aschenwald *et al.* 2001). The details of the transformations are not explicitly given by Aschenwald *et al.* (2001), who derived them from classical photogrammetry theory (Slama *et al.* 1980). This paper follows computer graphics theory, and for completeness and repeatability, the detailed procedure is explained in the following paragraphs.

Firstly, we select the visible portion of the DEM according to the angular field-of-view. This is derived from the focal length of the camera lens and the dimensions of the film. The angle ϕ in figure 1 is half the vertical field of view, and its value is:

$$\phi = \arctan \frac{(1/2)h}{f} \tag{1}$$

where f is the focal length and h is the vertical dimension of the film (24 mm for 35 mm standard photography). Similarly, the half value of the horizontal field of

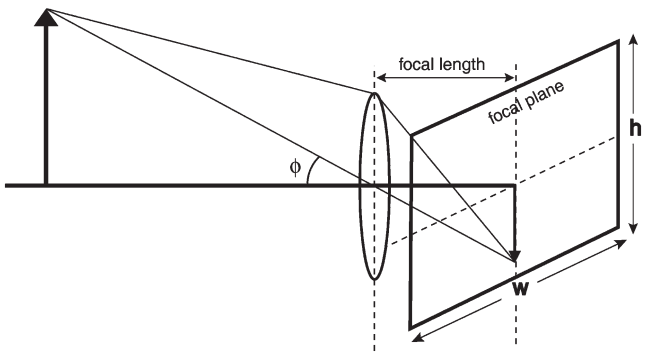

Figure 1. Simplified scheme of image formation in the camera. ϕ is half the angle of the vertical field-of-view, w is the width of the film (36 mm) and h is the height (24 mm).

view, φ, is:

$$\varphi = \arctan\frac{l}{2f} \tag{2}$$

where l is the horizontal dimension of the exposed film or 36 mm for this format.

Within this viewing window there are surfaces facing the observer and others facing away or hidden by nearer ground. These hidden surfaces are not seen by the camera, and in order to avoid duplicate or erroneous mapping of the photographic pixels to non-visible DEM cells a viewshed analysis was performed with ArcInfo, a commercially available GIS package. Future work will be carried out on the implementation of a viewshed algorithm by Wang *et al*. (2000), so that the whole procedure is a stand-alone routine coded in a single programming language.

Once visibility has been calculated, we apply a viewing transformation that maps points in the world coordinate system (that of the DEM) to points in the camera coordinate system, representing the viewing geometry of the camera in three-dimensional space, as shown in figure 2. A viewing transformation is parameterized by a viewing direction vector **N**, a vector **V** indicating which way is up, a vector **U** positive in the direction of the x-axis and a viewing position C (Fiume 1989). This is standard procedure for obtaining perspective views in computer graphics (e.g. Foley *et al*. 1990). First, we apply a translation transformation to set the origin at C, the camera position. The transformation matrix, in homogeneous coordinates, representing this translation, T_t would be:

$$\begin{pmatrix} P_{tx} \\ P_{ty} \\ P_{tz} \\ 1 \end{pmatrix} = \begin{pmatrix} 1 & 0 & 0 & -C_x \\ 0 & 1 & 0 & -C_y \\ 0 & 0 & 1 & -C_z \\ 0 & 0 & 0 & 1 \end{pmatrix} \begin{pmatrix} P_{wx} \\ P_{wy} \\ P_{wz} \\ 1 \end{pmatrix} \tag{3}$$

where P_w is any given point in world coordinates and P_t is the translated point to a reference system with origin at C, the camera position.

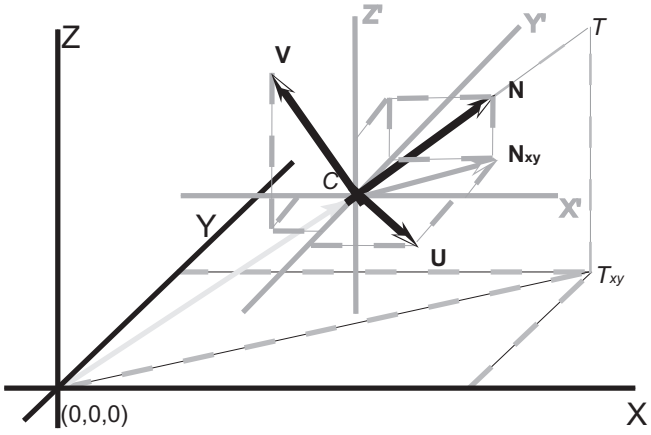

Figure 2. Change from world to camera coordinate system. DEM coordinates are referenced to the main reference system XYZ in the figure, while the image taken by camera at point C is referenced to the coordinate system defined by the three orthogonal unit vectors **UNV**. **N** is the viewing direction of the camera, calculated from the camera and target positions. **U** is the unit vector of the cross product of **N** and $\mathbf{N}_{xy}$, which is the projection of **N** on the horizontal plane. **V** is **UN**. **X′Y′Z′** is the translated reference system **XYZ** to point C.

Finally, the viewing transformation is completed by multiplying the result of equation (3) by the following transformation matrix, which rotates the translated coordinates according to the viewing reference system:

$$\begin{pmatrix} P_{cx} \\ P_{cy} \\ P_{cz} \\ \omega \end{pmatrix} = \begin{pmatrix} U_x & U_y & U_z & 0 \\ V_x & V_y & V_z & 0 \\ N_x & N_y & N_z & 0 \\ 0 & 0 & 1/f & 1 \end{pmatrix} \begin{pmatrix} P_{tx} \\ P_{ty} \\ P_{tz} \\ 1 \end{pmatrix} \tag{4}$$

where f is the focal length of the camera, ω is a scaling factor for the perspective projection (equation (9)), and P_c is the resulting coordinates of a point in the camera coordinate system.

The calculation of the unit vectors defining the viewing geometry is as follows. The viewing direction or vector **N** is:

$$\mathbf{N}_0 = T - C \tag{5}$$

$$\mathbf{N} = \frac{\mathbf{N}_0}{|\mathbf{N}_0|} \tag{6}$$

where T is the coordinates of the target (aim of the camera) and C the coordinates of the camera with respect to the DEM origin of coordinates.

From this vector, and applying a procedure slightly modified from that used by Fiume (1989) or Watt and Policarpo (1998), **U** and **V** are calculated using simple vector calculus, by finding the cross products:

$$\mathbf{U} = \begin{cases} \mathbf{N} \times \frac{\mathbf{N}_{xy}}{|\mathbf{N}_{xy}|} & \text{if } N_z > 0 \\ \frac{\mathbf{N}_{xy}}{|\mathbf{N}_{xy}|} \times \mathbf{N} & \text{if } N_z < 0 \end{cases} \tag{7}$$

$$\mathbf{V} = \mathbf{U} \times \mathbf{N} \tag{8}$$

where $\mathbf{N}_{xy}$ is the projection of **N** onto the horizontal plane, or (N_x; N_y; 0), and N_z the z coordinate of vector **N**.

After the viewing transformation a perspective projection is applied. This is a mapping function of the points in three-dimensional space to a flat two-dimensional space representing the window of the camera vision. A simplified geometry of the projection is shown in figure 3. Following Watt and Watt (1992) the resulting x, y coordinates are calculated as:

$$P_{px} = \frac{2fP_{cx}}{wP_{cz}} \text{ and } P_{py} = \frac{2fP_{cy}}{wP_{cz}} \tag{9}$$

where $P_{p(\mathrm{x;y})}$ are the new x, y coordinates of the perspective projection of the point $P_{c(x,\ y,\ z)}$ onto the projection plane, which in this case is the film. The factor 1/2 is introduced in the denominator to set the origin of the coordinates in the projection plane to the centre of the film.

The resulting set of x and y coordinates after the perspective projection recreate, at a lower resolution and at a different scale, the terrain surface captured by the film (figure 4). It is, in fact, a virtual photograph of the DEM. In order to map it to the original photograph it has to be scaled according to the resolution of the scanned picture. This is a simple linear transformation.

If the position of the camera and the viewing direction are correct, the projection of the DEM grid points should match the image in the photograph, as in

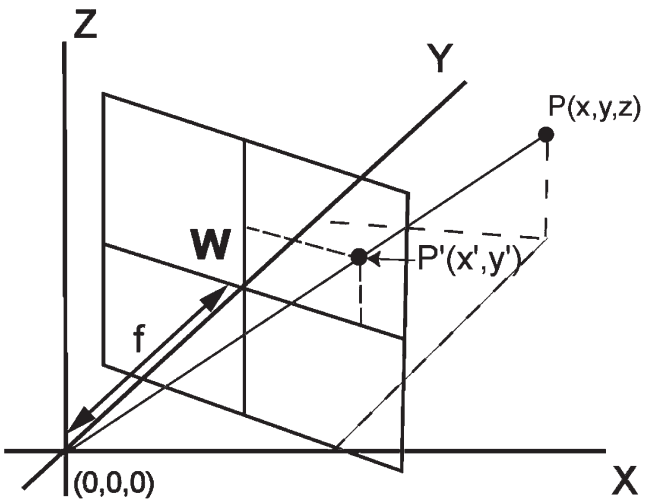

Figure 3. Simplified geometry of the perspective projection for one single point. A point P in tridimensional space is mapped (projected) to a point P' in a two-dimensional viewing window representing the camera film. The distance f to the origin of coordinates C in camera coordinate system is equivalent to the lens focal length. This perspective projection produces a virtual photograph of the DEM, which is then mapped to the pixels in the photograph. By conserving the link between P and P' the information in the flat two-dimensional photograph can be mapped to the original three-dimensional points in the DEM.

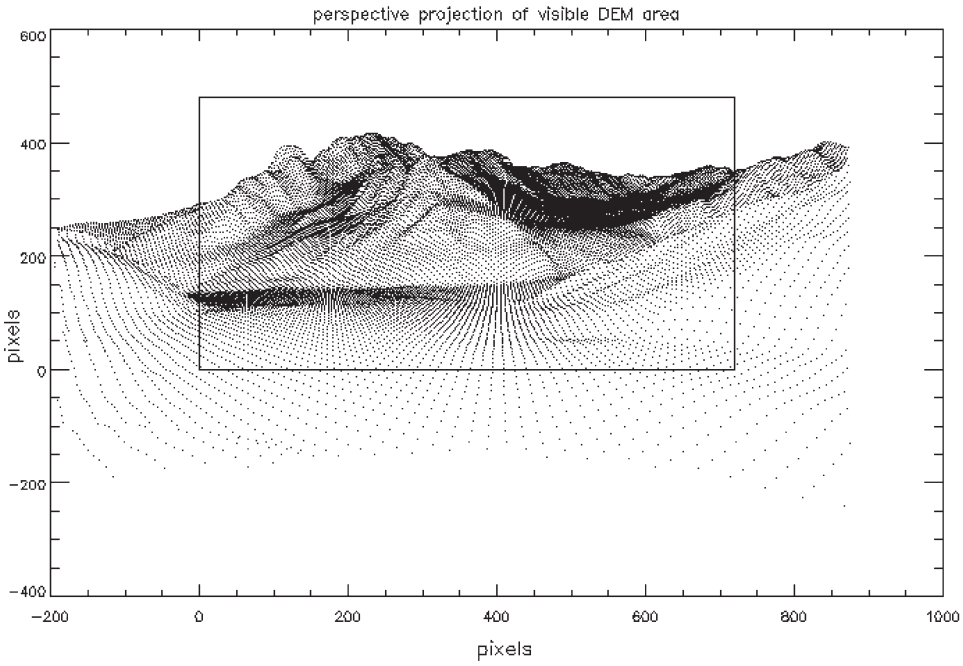

Figure 4. Perspective projection of a DEM of the lower section of the Mer de Glace, Mont Blanc. Every dot represents a grid cell after a viewing transformation and perspective projection. The frame is the camera field-of-view. Axis units are pixels in the original photograph: 720×480 within the frame, at a resolution of 200 dots per cm. $\mathbf{V}$ is $\mathbf{U} \times \mathbf{N}$.

figure 5, and the visual information of the picture can then be extracted and mapped onto the DEM. This is straightforward if, during the viewing and perspective transformation of the DEM, the link to the original coordinates of the grid cells is always preserved. When implementing the algorithm, this is attained by constructing a five-dimensional matrix with three dimensions (x, y, z) representing the original coordinates and two additional ones for those of the perspective projection.

Figure 4 shows the result of this perspective transformation, projection and scaling for a section of the Mer de Glace. The dots are the perspective projections of the original DEM grid cells, and the frame is the camera field-of-view. The photograph in figure 5 shows the superposition of the projected DEM (red dots) onto the original photograph. Green crosses are ground control points (GCPs), used for fast photograph orientation when the target coordinates are not precisely known and to assess the fitness of the match between the photography and the perspective projection of the DEM. If there were any uncertainty on the exact position of the point towards which the camera is aiming (the target), the viewing direction vector will not be precisely defined, and this will result in a displaced perspective projection of the DEM. In order to avoid the more lengthy computation of the whole DEM, it is sufficient to compute only a few well-defined GCPs to assess the accuracy of photograph orientation. Figure 6 shows a flow chart of the georeferencing process, where the first loop is done initially only for the GCPs in order to speed up the computation, and only when the match between GCPs and the corresponding points in the photograph is satisfactory is the process applied to the whole DEM.

Figure 5. Superimposition of the perspective projection of a DEM of the Mer de Glace (figure 4) over a photograph of the area. Red dots are the perspective projections of the original DEM grid cells, and green dots are the ground control points (GCPs). The GCPs are located on prominent points, such as the peaks on the ridge, and should be easy to identify on the image for fast photograph orientation. The photograph is taken from the Refuge du Requin looking east–north–east.

The end result of this first process is a georeferenced image of reflectance values, shown in figure 7. Reflectance in the case of visible photography refers to the three optical bands in the red, green and blue to which the film is sensitive, though the technique is of application to any other ground-based sensor able to record images in any spectral band. A more detailed georeferenced image, for the lower section of the glacier is shown in figure 8, in this case using a DEM resampled to 10 m resolution in order to show the potential of this technique to recognize and geolocate surface features.

3.1.1. *Photograph orientation*

Unless the camera is mounted on a theodolite or a similar apparatus, it is very difficult to keep its x-axis (vector **U**) in a strictly horizontal position at the time of taking the photograph, especially under adverse terrain and weather conditions. To

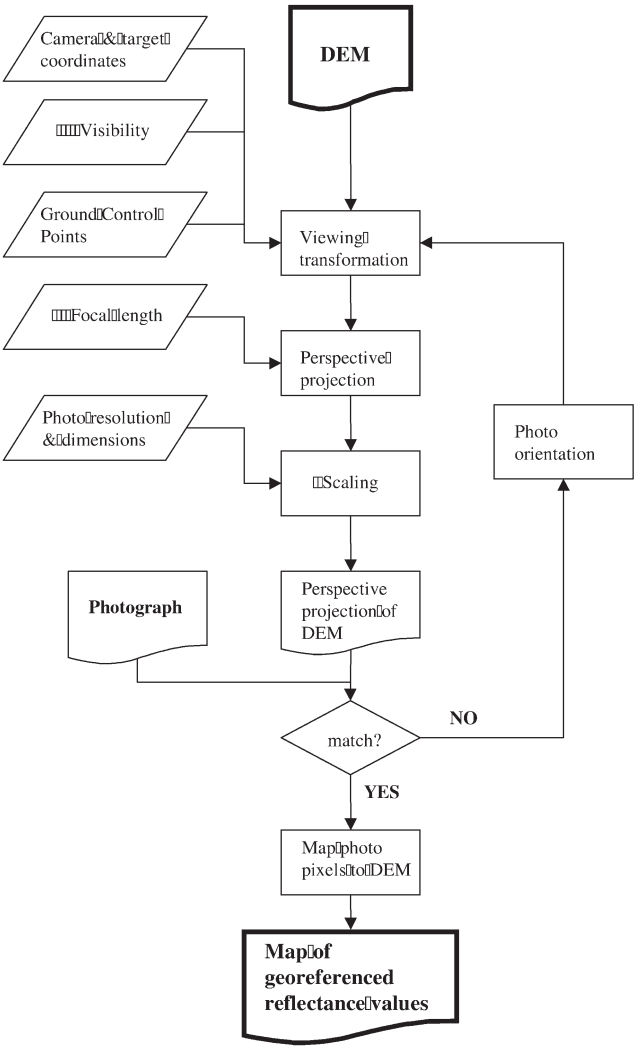

Figure 6. Flow chart of the georeferencing process.

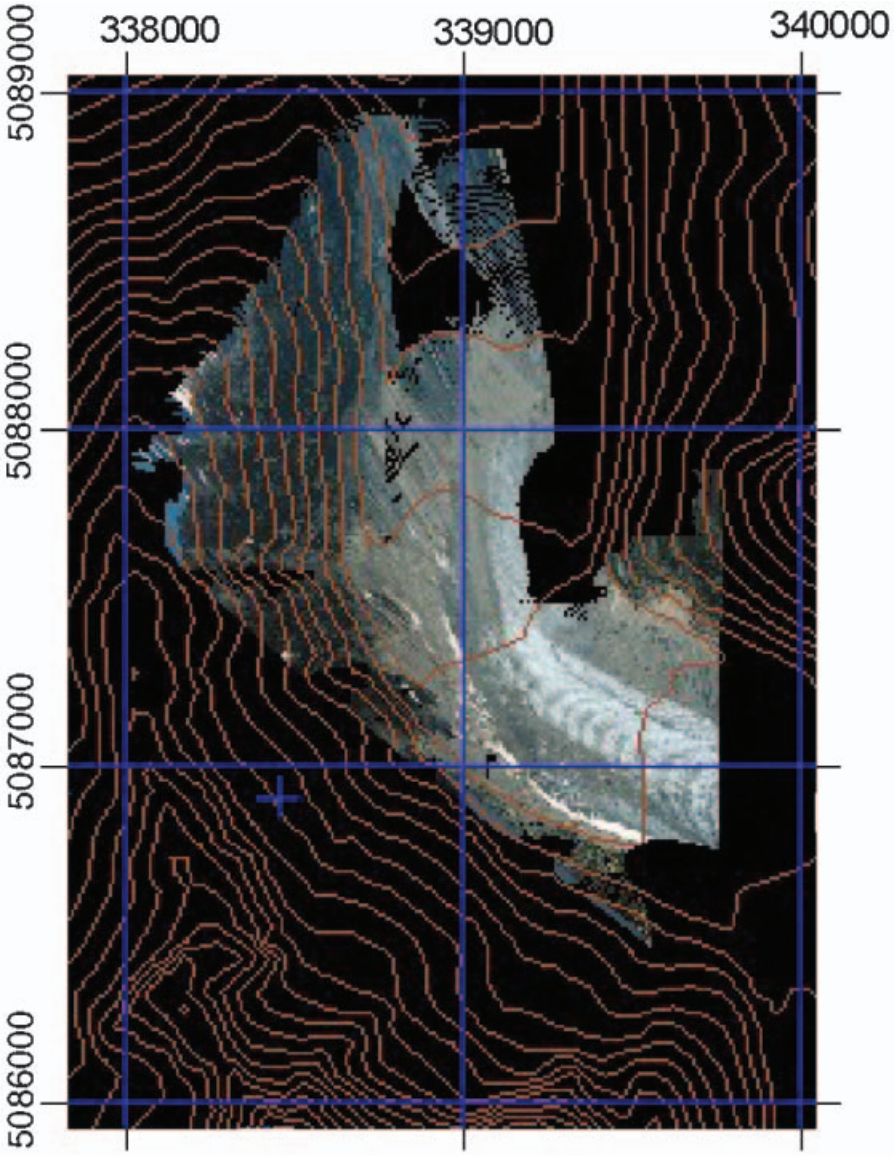

Figure 7. Georeferenced image of the lower middle section of the Mer de Glace. Reflectance values are extracted from the photograph in figure 5. Black areas (holes) are not visible from the camera position.

cope with this problem a simple algorithm for correction of camera rotation is implemented.

The simplest correction is for the distortion due to roll of the camera around the the viewing direction axis. Figure 9 shows the calculation of the angle of rotation. The discontinuous line represents the projected terrain points for a viewing coordinate system rotated approximately 15° anticlockwise (note that an anti-clockwise roll of the camera results in a clockwise roll of the image). The continuous line would be the photographed terrain. By measuring the pixel

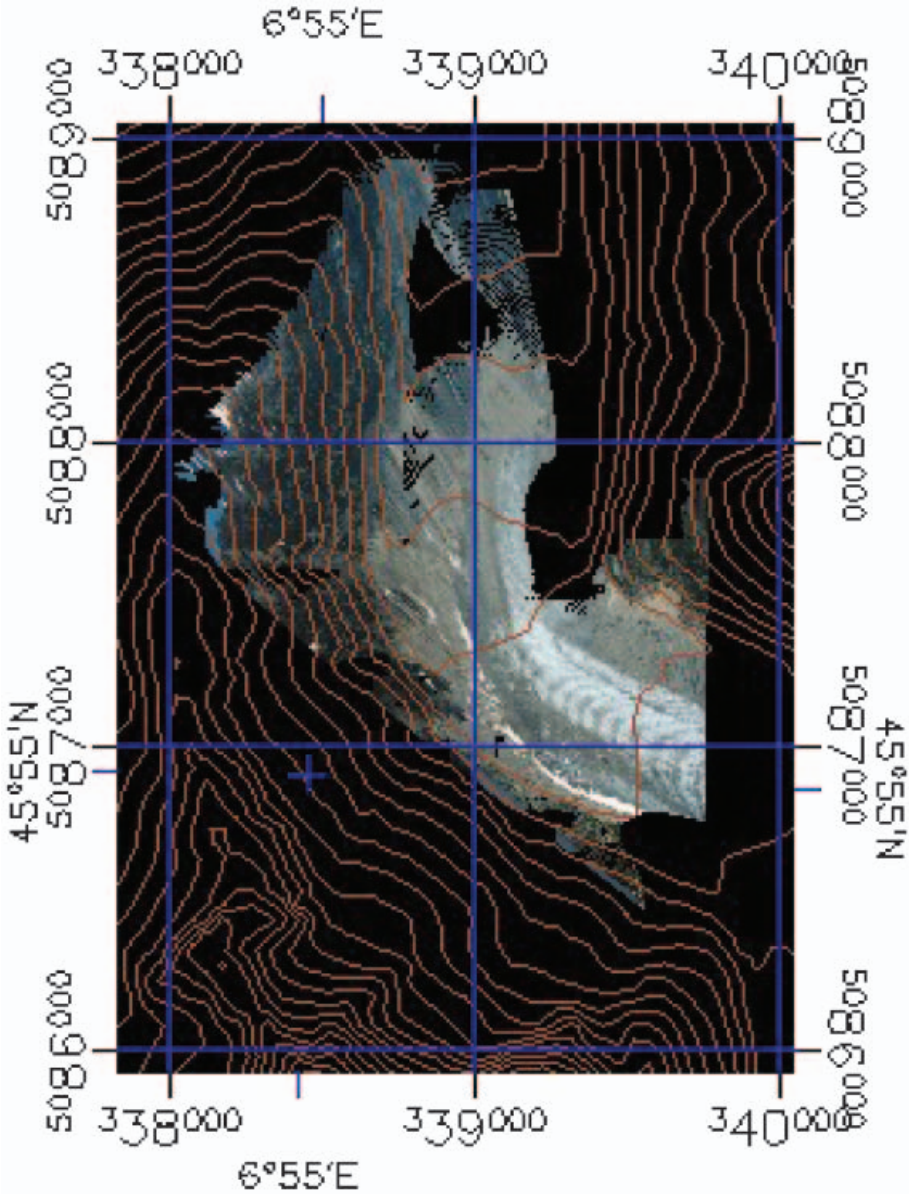

Figure 8. Detail of lower section of the Mer de Glace. Georeferenced image using a resampled 10 m resolution DEM to show the potential of this technique for landform and pattern recognition. Note the dark and white ojives or Forbes bands on the glacier, which are characteristic of the lower tongue of the Mer de Glace.

positions of both, the actual image P_i and the projected elevation points P_p relative to the centre of the image, we can calculate angles ψ and γ and their difference, which is angle ζ, the actual roll of the camera. By rotating the camera coordinate system $C\mathbf{UVN}$ an angle ζ, the distortion due to roll is corrected. As we are dealing with unit vectors, the operation is reduced to adding a vertical vector of

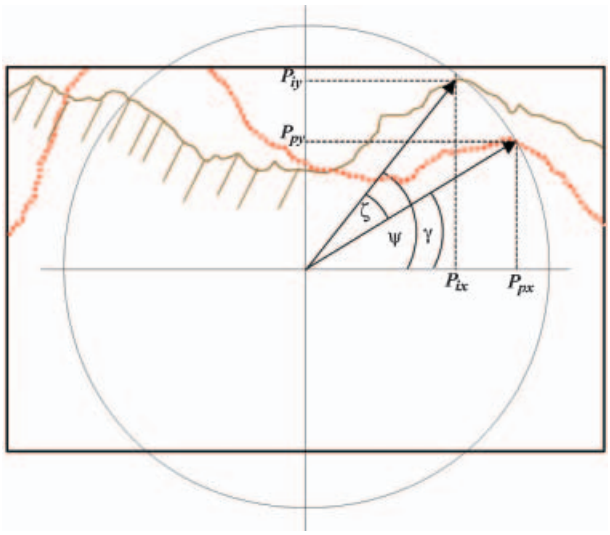

Figure 9. Example of mismatch between the perspective projection of the DEM (dotted line) and the photographic image (continuous line) due to roll of the camera. The correction for this displacement is explained in § 3.1.1.

magnitude—tan ζ to **U** (recall from equation (7)) and finding the unit vector in the resulting direction:

$$\psi = \arctan\frac{P_{iy}}{P_{ix}} \tag{10}$$

$$\gamma = \arctan\frac{P_{py}}{P_{px}} \tag{11}$$

$$\zeta = \psi - \gamma \tag{12}$$

$$\mathbf{u}_\zeta = (0,\, 0,\, -\tan\zeta) \tag{13}$$

$$\mathbf{U}' = \frac{\mathbf{U} + \mathbf{u}_\zeta}{|\mathbf{U} + \mathbf{u}_\zeta|} \tag{14}$$

$$\mathbf{V}' = \mathbf{N} \times \mathbf{U}' \tag{15}$$

The new, rotated camera coordinate system will be $C\mathbf{U}'\mathbf{V}'\mathbf{N}$.

The differences between expected (due only to rotation) and measured values of the displacement of P_p along the x-axis will give us information on the yaw of the camera, or horizontal displacement of the estimated target. Extensive work has been done towards the elaboration of precise photograph orientation algorithms (e.g. Croitoru and Ethrog 2001), although it was found that the use of precise ground control points, for example, collected by differential GPS (global positioning system), allows fast manual photograph orientation by trial and error.

3.1.2. *Additional corrections*

Additional corrections to account for the curvature of the Earth and the refraction of light through the atmosphere need to be taken into account in some cases. Curvature of the Earth may be important for images taken from a long

distance. Simple trigonometry shows that the depression of the observed point or dip (Δz) is related to the distance to the observer by:

$$\Delta z = R_e - \frac{R_e}{\sqrt{R_e^2 + d^2}} \tag{16}$$

where R_e is the radius of the Earth (mean value: 6 367 450 m) and d is the distance to the observer. For example, for a distance of 10 km the dip would be 7.85 m, which should be subtracted from the cells' heights at that range prior to the georeferencing process.

The refraction of light is only important for paths through the atmosphere where the target and the observer are at very different altitudes, and therefore at significantly different air densities. Refraction is evaluated using the MODTRAN radiative transfer model (Berk *et al.* 1989). In the present study, for typical atmospheric conditions and maximum difference in height, the cumulative bending of the light rays is about 0.012°, which for the maximum distance range within the DEM amounts to an error of 2 m. However, the photographs are taken for smaller areas and elevation ranges, which made refraction and curvature in this case negligible.

Radial distortions are highly variable depending on the quality of the lenses used. This type of distortion alters the geometry of the image, typically in an exponential way as we move away from the centre of the image. Access to this information is not easy, as manufacturers normally classify it as confidential, but typical values are in the range of up to tens of μm (Cooper and Robson 1996, Fryer 1996). For a scanned digital image at 200 dots per cm (512 dpi), the radial distortion would be smaller than one pixel, and therefore negligible. An alternative solution if the radial distortion is expected to be high is to discard the margins of the photograph and cover the area with another photograph centred around the discarded area. Tangential distortion is typically small compared to radial distortion (Jacobson 1978).

Other errors due to coma, astigmatism, barrel and pincushion distortion of the lens, curvature of field (Jacobson 1978) and for film deformation due to unflatness (Fryer 1996) are minimized by using high-quality lenses and cameras.

3.2. *Conversion from reflectance to albedo*

A pixel in a photograph contains information on the reflected radiation coming from a determined surface area. This reflected radiation will depend on the incoming global radiation, the albedo of the surface, the intervening atmosphere and the viewing geometry. The global radiation is the result of multiple interactions of the solar radiation field with the atmosphere, the target and the surrounding terrain. Thus, the main factors affecting the solar radiation falling on a surface are:

(a) Ratio of direct to diffuse radiation.
(b) Angle of incidence of the solar beam on the surface.
(c) Local horizons to the surrounding ground and the nature of this ground.
(d) Fraction of visible sky in the upper hemisphere, or skyview factor.
(e) Multiple scattering of solar radiation between the sky and the ground.

The main factors affecting the measurement and recording of reflected solar radiation arriving at the film are:

(1) Atmospheric transmittance between the object and the camera.

(2) Anisotropy of the reflected radiation.
(3) Input/output relationship between the incoming light and the response of the lens-camera-filmscanner system.

A photograph contains a large amount of information at a very high resolution, but it is not a system designed for retrieving quantitative information from the original incoming radiation. However, this work assumes that there is a direct relationship between the albedo of a surface and the camera output of the recorded reflected flux radiance. Then, by comparing the values of pixels in a photograph to a determined reference pixel corresponding to a surface of known albedo, we can estimate the albedo of the remaining surfaces, even when it is not possible to estimate the actual value of the radiative flux arriving to the film.

The surface albedo is defined as the ratio of the hemispheric reflected (I_r) and incoming (I_i) radiative fluxes (e.g. Knap and Reijmer 1998):

$$\alpha = \frac{I_r}{I_i} \tag{17}$$

The incoming radiative fluxes are calculated as:

$$I_i = r I_{sc} \tau i (F_t + F_{sk} + F_{ms} + F_{sn}) \tag{18}$$

where I_{sc} is the solar constant or 1367 Wm^2; r is the reciprocal of the square of the radius vector of the Earth, or correction for the eccentricity of the Earth's orbit, which here is calculated using Fourier series derived by Spencer (1971); and τ_i represents atmospheric transmittance functions, for both diffuse and direct radiation, which take into account Rayleigh scattering, transmittance by ozone, by uniformly mixed gases, by water vapour and by aerosols. These functions are computed following a parametric model by Iqbal (1983). The τ-functions incorporate the relative optical path length and pressure-corrected air mass, depending on solar zenith angle and altitude. Further updates to Iqbal's model are introduced for the calculation of precipitable water, following Prata (1996), and for increased transmittance with altitude, in accordance with values recommended by Bintanja (1996). The ozone layer thickness is extracted from the NASA Total Ozone Mapping Spectrometer dataset (TOMS-EP 2001).

The model has been tested successfully at high altitude in the Andes by the author (Corripio and Purves 2004), where the differences between modelled and measured data were smaller than the error introduced by pyranometer accuracy (3%), and gives the best results in a comparative study of radiative flux parameterizations for shortwave radiation published by Niemelä *et al.* (2001).

The terms of the last factor in equation (18) represent the corrections for the influence of topography and diffuse radiation. These are:

$$F_t = f_{dt} \mathbf{n} \cdot \mathbf{s} = f_{dt} \cos\theta_s \tag{19}$$

is a correction term for the angle of incidence of sun on the slope, where f_{dt} is the ratio of direct to total incoming radiation, $\mathbf{n}$ is the unit vector normal to the surface and $\mathbf{s}$ is the unit vector in the direction of the Sun. This dot product is equivalent to the cosine of the relative solar zenith angle θ_s. F_t is computed only for cells in the sun, not in the shadow.

$$F_{sk} = f_{dt} f_v \tag{20}$$

is diffuse radiation from the sky, f_{dt} is the ratio of diffuse to total incoming

radiation, calculated from Iqbal's model, and f_v is the hemispherical fraction of visible sky, or skyview factor. f_v and **n** are calculated from a DEM of the area; these two terms and **s** are computed following Corripio (2003).

$$F_{ms} = \alpha_{sk}\left(f_s\alpha_s + (1-f_s)\alpha_g\right)f_{sh} \tag{21}$$

is diffuse radiation due to multiple scattering between the ground and the sky, where α_{sk} is the albedo of the atmosphere, which depends on atmospheric conditions and is calculated according to Iqbal (1983); f_s is the fraction of surrounding terrain covered by snow with albedo α_s; the remaining terrain has an estimated albedo of α_g; and f_{sh} is a shadow factor:

$$f_{sh} = f_{dr}f_{st} + f_{df} \tag{22}$$

where f_{st} is the ratio of cells in the sun to total number of cells.

A rigorous computation of reflected diffuse radiation will require an exhaustive evaluation of viewing geometry and illumination conditions of the surrounding terrain, which is computationally expensive. Therefore, a simplified approach is suggested in the form of the following equation:

$$F_{sn} = (1-f_v)\left(f_{sv}\alpha_s + (1-f_{sv})\alpha_g\right)f_{sh} \tag{23}$$

where the term f_{sv} is the ratio of snow covered to total visible surrounding terrain. Following Greuell *et al*. (1997), a distinction is made between f_s and f_{sv}, as reflected diffuse radiation from snow will come from those surfaces which are visible, while the diffuse radiation due to multiple scattering with the sky might come from surrounding snow-covered terrain which is not visible from the area under consideration.

The snow albedo is not isotropic, and variations might be important, especially at low relative solar zenith angles. It is generally agreed that the albedo of the snow is independent of θ_s for θ_s smaller than 50° (Wiscombe and Warren 1980, Brock *et al*. 2000). In any other cases, and for the albedo of the ice, bidirectional reflectance distribution functions should be applied (see for example: Greuell and de Ruyter de Wildt 1999, Knap and Reijmer 1998).

The reflected radiation arriving at the camera or recording device per pixel will be:

$$R = I_i\alpha\Omega\tau_t \tag{24}$$

where Ω is the ratio of the solid angle of a receptor's pixel field-of-view to 2π (the whole hemisphere solid angle), and τ_t is a transmittance function to account for atmospheric attenuation between the target and the camera. τ_t is calculated using MODTRAN and general knowledge of the local atmospheric conditions. Running the MODTRAN model for all the cells would be extremely time consuming if not impossible. Thus, a feasible solution is to run the model for a set of points containing the boundaries of the DEM, clusters of points in the regions of more interest and randomly selected points. From the results of these runs, a statistical fit is interpolated as a surface of minimum curvature passing through the given values. Transmittances for all the remaining grid cells are obtained by reference to this interpolated surface.

The ratio of the reflectance of any given pixel R_n to a reference pixel reflectance R_{ref} whose albedo is known, will be:

$$\frac{R_n}{R_{ref}} = \frac{(I_i\alpha\Omega\tau_t)_n}{(I_i\alpha\Omega\tau_t)_{ref}} \tag{25}$$

Rearranging terms, combining with equation (18) and noting that $\Omega_n = \Omega_{ref}$, as the camera pixels are uniform and their field of view solid angles are identical, we have:

$$\alpha_n = \alpha_{ref} \frac{R_n}{R_{ref}} \frac{(\tau_i \tau_t)_n (F_t + F_{sk} + F_{ms} + F_{sn})_{ref}}{(\tau_i \tau_t)_{ref} (F_t + F_{sk} + F_{ms} + F_{sn})_n} \tag{26}$$

where $(\tau_i)_n$ and $(\tau_i)_{ref}$ may cancel each other if altitudinal variations within the area under consideration are small.

The ratio R_n/R_{ref} is calculated directly from the digital numbers of the digitized (scanned) photograph. α_{ref} is known by direct measurement and the remaining terms are calculated following equations (18) to (23). Thus, it is sufficient to know a reference albedo, which is measured at one single point, in order to estimate the albedo of the whole area in the image. If no direct measurement of a reference point is possible, then a surface on known reflectance such as a Kodak grey card or a spectralon panel could be introduced at the time of taking the image and then the same procedure could be followed to calculate the albedo of the remaining pixels.

3.2.1. *Narrow band versus broadband albedo*

The recording device used in this work is slide film for visible light, sensible to radiation in the range of 400–700 nm. However, the snow absorbs energy in the form of shortwave radiation in a wider spectrum, and the albedo is generally measured in the range 300–2800 nm. A conversion between the narrow visible band to the wide shortwave band is desirable.

Snow may show a large variation in albedo in the near infrared, depending mainly on snow grain size (Wiscombe and Warren 1980, Dozier *et al*. 1981). However, the corresponding variations in the visible band are too small to detect with normal photographic film. Therefore it is not possible to extend the visible albedo to a wider band using only information on the visible range. According to MODTRAN model outputs, the actual energy inputs in the regions 300–400 nm and 700–2800 nm, for the usual atmospheric conditions in which we were working, are 10% and 25% respectively of the total shortwave energy. The maximum range of albedo variation is very small in the ultraviolet and up to approximately 40% in some regions of the infrared for varying snow grain size (Wiscombe and Warren 1980, figure 9). Thus, the maximum error in the estimation of energy inputs in the case of extreme variations of snow grain size, considering only the visible band, would be about 9% and typically smaller. During the present work snow grain size was practically uniform over the whole area except for the upper section of Mont Blanc de Tacul, above 4000 m a.s.l. The size of the snow grain was determined on the field by observing the snow under a magnifying glass over a graduated ruler. Ground above 4000 m represented only 2% of the total surface and images used for the computation normally contain only one uniform type of snow. Therefore, the extension of albedo values derived from reflectance comparisons in the visible region band to broad band albedo is a reasonable assumption in this particular case. Further research will focus on ways of improving the estimation of albedo by using digital or spectral cameras sensitive to near-infrared radiation.

3.2.2. *Film-scanner input/output relationship*

The relationship between incident light on the camera and film response depends on the emulsion used, the type of lens, the exposure, brightness of the object and film development. Additionally, the accurate response of the scanner to

the light transmitted through the processed film is difficult to quantify, as scanner manufacturers normally do not provide the necessary information. These processes introduce uncertainties and non-linearities in the evaluation of the scanned digital image.

An empirical approach was followed to deal with this problem, to obtain a function that relates input (incoming light) to output (digital values produced by the scanner) for a given combination of lens-film-scanner. The procedure is similar to sensitometric analysis in photography (Jacobson 1978) and consists of finding a statistical fit between known illumination values and resulting output from the scanner.

In the present work a graded grey-scale card (Kodak Grayscale Q-13) was photographed and used as a calibration input. This card is a rectangle divided into 25 boxes of varying shades of grey, from near white to near black at 0.05 density steps, from nominal values of 0.05 to 1.95. Density is a magnitude normally used in photography, whose value is the logarithm of light flux intensity, either transmitted through the film or reflected from a surface. Thus, the grey-scale card densities correspond to reflectance values between 1% and 89%. Values below 10% were ignored, because the response of the film in this area is nonlinear and we are dealing with snow, which always has a higher reflectance. Values for the scanned test photograph are plotted in figure 10. Most photographic films present characteristic response curves that show a straight line between a toe of increasing slope in the darker region of the image and a shoulder of decreasing slope near saturation. Therefore, a correctly exposed film, with density values within these two thresholds, should present a linear response, although slightly modified by the development and scanning. For a film scanned at gamma = 1, figure 10 shows a linear relationship

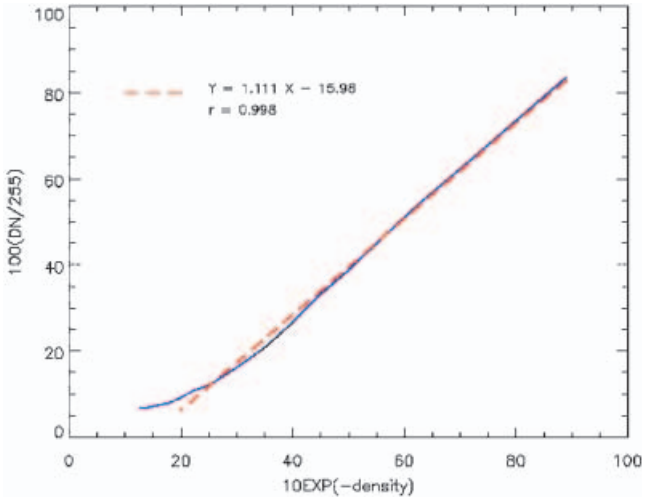

Figure 10. Digital Number (DN) versus reflectance. The output of the scanned photographic image is conditioned by the whole photographic process, camera, lenses and scanner characteristics. In order to relate the input light to the output values an empirical approach was followed. The solid line shows the relationship between input light and output DN values, and the dashed line is a regression fit excluding areas of very low reflectance. The regression is then linear, and the exclusion of very low (dark) values is justified as we are dealing with snow, with high reflectance values, in the region where the function is linear.

close to 1:1 (slope = 1.111, $r^2 = 0.998$, which for the number of measurements available gives a confidence level higher than 99.5% according to tabulated values of the *t*-test) for digital numbers corresponding to reflectances in the snow region. This linear relationship simplifies the correction between original reflectance values and the DN values produced after scanning the film. It is sufficient to solve for the x in the regression equation and apply it to the reflectance values.

3.3. *Data format*

To facilitate data portability and to integrate DEMs and image files, the GeoTIFF data format was chosen for digital analysis and storage. GeoTIFF represents an effort by over 160 different remote sensing, GIS, cartographic, and surveying-related companies and organizations, to establish a TIFF-based interchange format for georeferenced raster imagery (Ritter and Ruth 1997, 2000).

4. Experimental set-up

Photographs and direct albedo measurements were taken on the Mer de Glace on different days from 6 to 26 June 2000. The Mer de Glace is the largest glacier in the French Alps and the third largest in the whole Alps (figure 11). It is located east of Mont Blanc, with a length of 12.3 km, and a surface area of 32.09 km^2 (Hoelzle and Haeberli 1999). The altitude ranges from 4248 m a.s.l. down to 1470 m a.s.l. The location was selected taking into account the variability of snow and ice surface albedos, different orientations, accessibility, safety and efficiency of time allocation.

The azimuth of the principal glacier slopes range from 0 to 180°, with the largest sections of the glacier facing south, south-east and north. This range of orientations makes it possible to study the glacier at different times and with different solar illumination conditions. The upper section of the glacier, above 4000 m, had fresh snow that had not suffered intense metamorphism processes, and consequently had a higher albedo. However, most of the glacier was covered in well-metamorphosed granular snow. The lower section was bare glacier ice partially covered in debris.

Albedo measurements were taken using a CM 7B albedometer (Kipp & Zonen, Delft, The Netherlands), which consists of two opposed pyranometers sensitive to hemispherical incoming and reflected short-wave radiation in the range 300–2800 nm. The albedometer was attached to a photographic camera tripod, as shown in figure 12, and positioned parallel to the surface to minimize measuring errors due to the inclination of the surface (Mannstein 1985, Sicart *et al.* 2001). Measurements were taken on the widest possible range of surface types, orientations and time of the day. The location of every site was determined using a GPS with a nominal precision of 15 m. The actual precision, especially at the bottom of the valleys with poor satellite visibility and geometry was estimated to be in the range of 25–100 m by comparison of actual readings on the GPS receiver with points whose locations were well known.

A DEM at 50 m grid resolution was purchased from the French Institute Géographique (Paris). Photographs were taken with a Nikon F4 camera (Nikon, Tokyo) and lenses in the range 35–80 mm. The film used was Kodak Ektachrome E100SW for visible light, which shows a good overlapping of spectral bands and extended linear response over its sensitivity range (Kodak 2001). A Kodak grey card was used as a reference card, both for the intensity of reflected light and for spectral balance. Although the grey card is not a perfectly diffuse reflector, it has

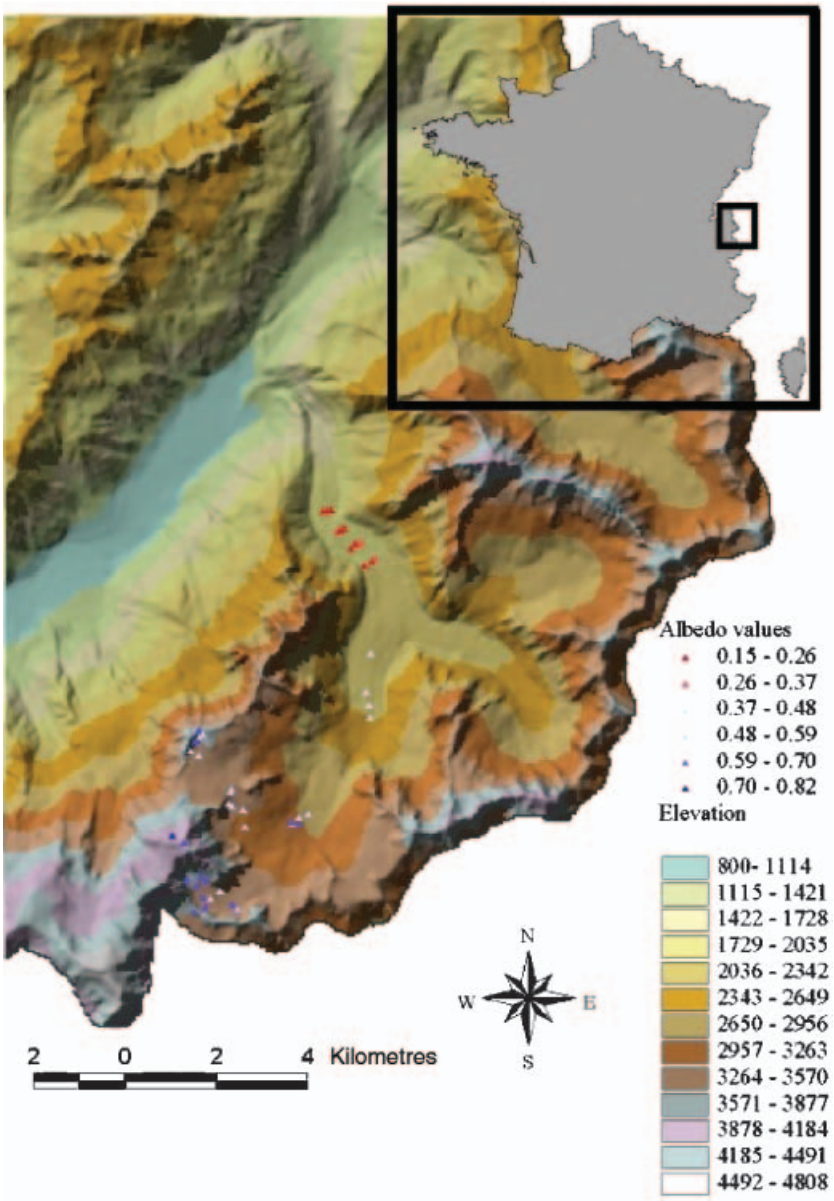

Figure 11. Map of the area of study in the French Alps, 45° 50′ N, 7° E. The Mer de Glace is the inverted Y-shaped glacier in the lower centre of the image. Coloured dots are albedo measurements. The DEM only covers the French side of the area, with no values for Italy and Switzerland.

small variations in reflectance over the optical wavelengths according to Milton (1989) and to tests with a GER 3700 spectrometer performed by the author.

5. Results and discussion

The results of the georeferencing process for this test site have already been introduced in § 3.1, figures 7 and 8. The accuracy of the georeferencing process

Figure 12. Albedometer setting. The white oval, above and right of the camera tripod, is the albedometer, made up of two Kipp & Zonen opposed pyranometers. The output is read in two voltmeters connected at the extreme of the cable in the bag below the skier-operator in the image.

decreases with shallow viewing angles (areas of closely packed red dots in figure 5), and is better for viewing directions approaching the normal. This fact makes the technique more appropriate for mountainous terrain, where images can be taken from ridges and peaks with steep viewing angles to the valley.

The final result of the albedo estimation is shown in figure 13 as a colour-coded georeferenced composite image of estimated albedo values derived from three different photographs of the Mer de Glace. Coloured crosses representing the measured values are superimposed, so that discrepancies can be easily highlighted, although none is obvious in this case. The inset, extracted from a resampled DEM at higher resolution, is a detail of the lower section, showing the albedo variations among the glacier ojives (glacier ojives or Forbes bands are alternating, arcuate bands of darker and clearer ice due to differential seasonal debris accumulation when the glacier traverses an icefall). Black areas are either areas non-visible from the photograph or with relative solar zenith angles higher than 60°. Figure 14 shows the differences between estimated and measured albedo values. The maximum error in the estimation of albedo is 6.5%, while the average error is only 2.2%.

In general, errors are small and most of them are derived from displacements between photograph and DEM during the georeferencing process, especially in

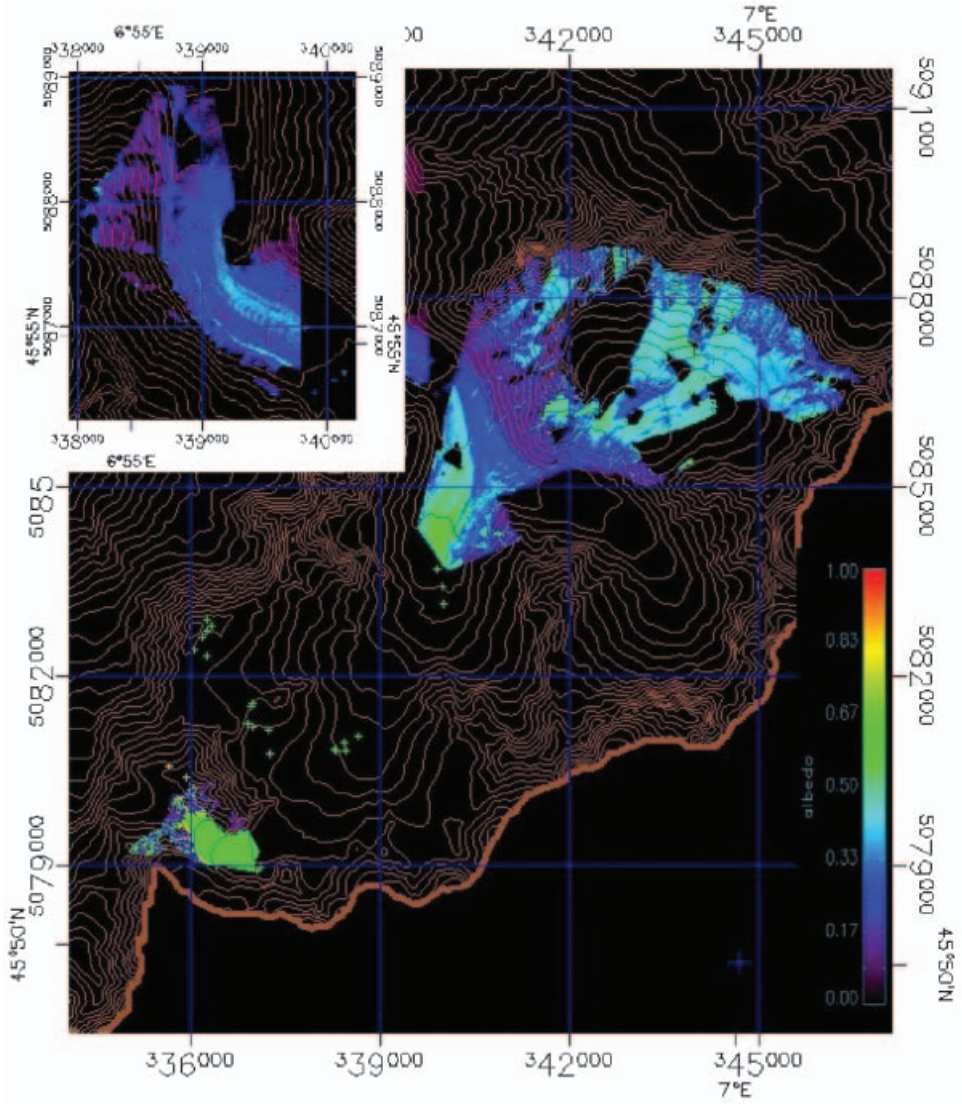

Figure 13. Colour coded composite map of albedo values derived from three georeferenced photographs of the Mer de Glace. Coloured crosses are measured values, a first inspection reveals good agreement between measured and estimated values. Actual values are plotted in figure 15. The inset is a detail of the lower section of the Mer de Glace, corresponding to figure 8, showing the albedo variability among the glacier ojives.

areas where there is an abrupt change of slope. This is because the angle between the sun and the normal to the slope is the most important parameter affecting the conversion between reflectance values and albedo. Thus, a small displacement may cause a relatively flat pixel to be corrected for an excessively steep slope. This type of error can be avoided, improving the georeferencing process by providing a more precise and larger number of ground control points. Uncertainties in the exact geolocation of the photographic-pixels, together with ambiguous assignation of image pixels to DEM cells, especially for low resolution DEMs, may lead to errors

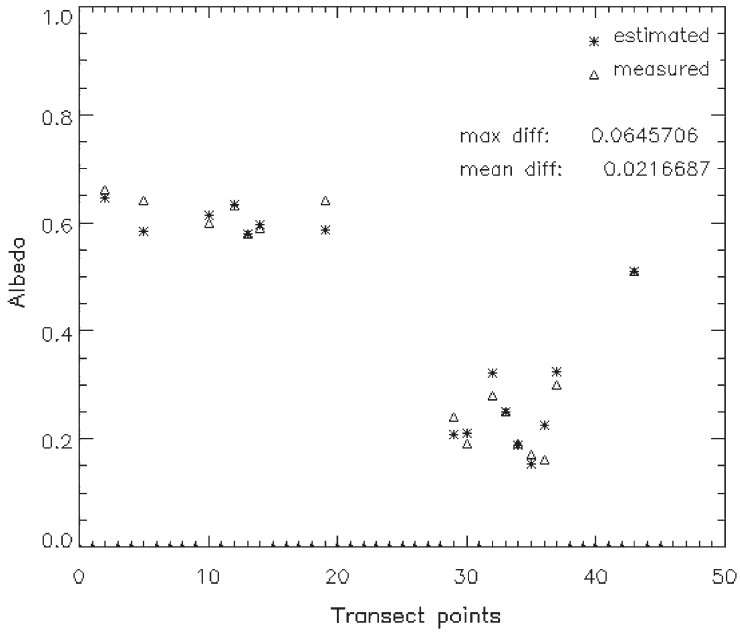

Figure 14. Measured versus estimated albedo values for areas in figure 13. The maximum difference is 6.5%, while the average is 2%, which is less than that of the albedometer. Measured points on the *x*-axis are ordered from west to east.

due to high albedo variability over the glacier. As figure 15 shows, the inter-pixel variability of albedo values is in the same range as the maximum error in the albedo estimation. This variability is at a maximum in areas partially covered with debris and on patchy surfaces, with intermixing of snow and glacier ice. The date of DEM production is important too, given the fast retreat and thinning rate of some Alpine glaciers.

When using normal film and additional scanning of the image on non-metric cameras, there is always some mismatch between the actual borders of the film and the origin of the image. The film was scanned using a Nikon Coolscan film scanner, with the film mounted in such a way that the lower left corner of the image could be clearly identified. Additional attention must be paid if the film is scanned from a framed slide, as there may be some additional inaccuracies due to internal displacements of the film inside the slide mount. Additionally, the corners of the photographic emulsions are not perfectly square (Croitoru and Ethrog 2001), which may add an uncertainty of a few pixels, reducing the accuracy of the georeferencing step. This problem can be easily solved using digital photography.

As there was limited information on the anisotropy of the reflected solar radiation over the snow, the traditional rule of thumb that considers albedo to be independent of the relative solar zenith angles for angles smaller than 50° (Wiscombe and Warren 1980) was applied, and cells falling outside this condition were masked out. Work by Greuell (2002) shows that there is still insufficient knowledge about the angular distribution of the reflected radiation over the snow and that bidirectional reflectance distribution functions (BRDFs) may not be of universal application. Therefore the masking out option was considered safer than applying corrections from BRDFs derived at other locations and with different

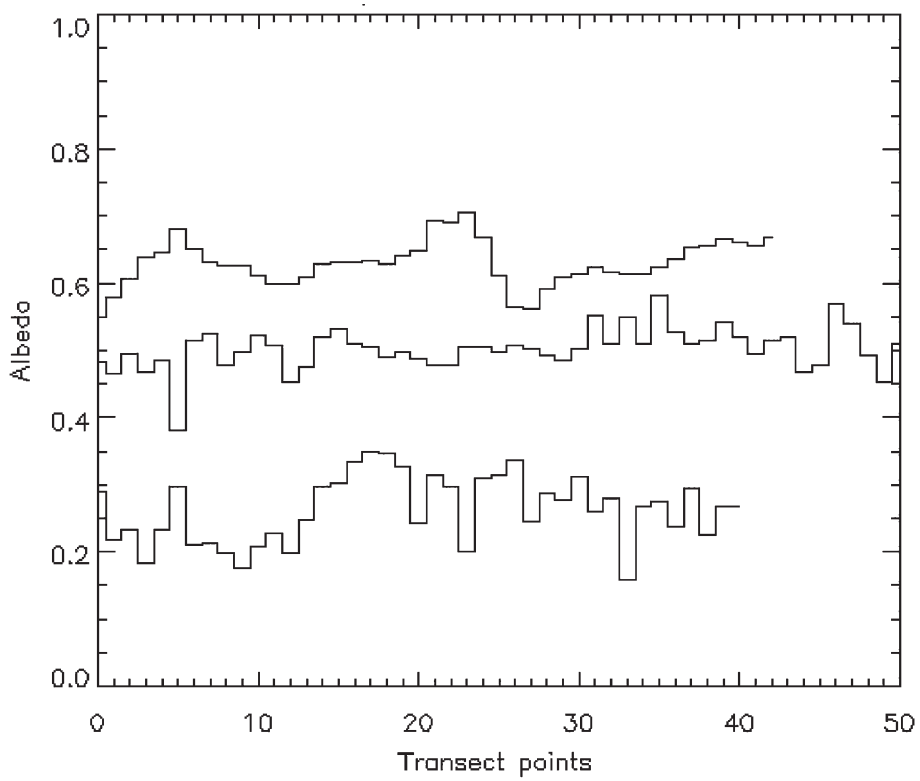

Figure 15. Inter-pixel variability of the albedo values for three arbitrary transects on the upper, medium and lower (ice covered) areas of the glacier. High variability in a relatively small space is a large source of error in the photography-derived albedos.

snow characteristics. A further project using a modified application of the photographic technique described in this paper for the derivation of suitable BRDFs is under consideration. Albedo was estimated only for the visible part of the spectrum, which may lead to some errors (see § 3.2.1), although the uniformity of grain size in the case study suggests that these errors are likely to be small.

6. Conclusions and outlook

Two complementary techniques are described in this paper. The first one, georeferencing of terrestrial photography, is a flexible and inexpensive remote sensing tool that has potential applications in many environmental and monitoring fields, such as: snow mapping, vegetation surveys, erosion monitoring, geomorphological mapping and visualization in GIS, and may improve previous applications of photography to land cover mapping and change monitoring (e.g. Christiansen 2001). It provides an economical tool to assess any kind of land cover change at a high temporal resolution, with a spatial resolution and accuracy limited only by the scale and quality of the available DEM. It is, in summary, a flexible and inexpensive remote sensing tool.

The second technique is a simple and effective way of estimating the distribution of snow surface albedo from one single reference measurement. This may improve the implementation of distributed snow energy balance models, and in glaciated

areas reduces the exposure of field workers to potential risks such as crevasses and avalanches. The present work has some limitations due to the limited spectral sensitivity of the photographic film used and the uncertainties in the anisotropy of the albedo.

Further work using a higher resolution DEM and GCP collection with differential GPS would be desirable in order to assess the precision of the georeferencing process and to minimize the errors in albedo estimation due to geolocation. The use of a spectral digital camera may produce enough data to find a suitable algorithm for the conversion of narrow band photography to broad band albedo, similar to those applied to satellite-derived albedos (Knap *et al*. 1999, Greuell *et al*. 2002). Finally further tests with a narrow field-of-view on different types of snow and different illumination and viewing angles would be desirable to test and implement suitable bidirectional reflectance distribution functions to correct for the anisotropy of the reflected solar radiation field.

Acknowledgments

Fieldwork was supported by a grant from Kodak (Research and Development), Harrow, UK. I would like to thank Research Systems Inc. (Boulder, CO) for their support with IDL software. This project was carried out while enjoying a Carnegie Scholarship at Edinburgh University, UK. I would like to express my gratitude to Ben Brock, Dundee University, UK, for the lending of an albedometer; to Chamonix mountain guide Ricardo Mora for his support during fieldwork; to him and his family for their hospitality in the Alps, and to the Chamonix Meteorological Office for kindly providing meteorological data. I am grateful to Ross Purves and Nick Hulton for useful suggestions that greatly improved this paper. I would like to acknowledge an anonymous referee whose comments improved the clarity and quality of the final manuscript.

References

ASCHENWALD, J., LEIGHTER, K., TASSER, E., and TAPPEINER, U., 2001, Spatio-temporal landscape analysis in mountainous terrain by means of small format photography: a methodological approach. *IEEE Transactions on Geoscience and Remote Sensing*, **39**, 885–893.

BERK, A., BERNSTEIN, L. S., and ROBERTSON, D. C., 1989, MODTRAN: A Moderate Resolution Model for LOWTRAN 7. Technical Report GL–TR–89–012, Air Force Geophysics Laboratory, Hanscom Field, MA.

BINTANJA, R., 1996, The parameterization of shortwave and longwave radiative fluxes for use in zonally averaged climate models. *Journal of Climate*, **9**, 439–454.

BROCK, B. W., WILLIS, I. C., and SHARP, M. J., 2000, Measurements and parameterization of albedo variations at Haut Glacier d'Arolla, Switzerland. *Journal of Glaciology*, **46**, 675–688.

CHRISTIANSEN, H., 2001, Snow-cover depth, distribution and duration data from northeast Greenland obtained by continuous automatic digital photography. *Annals of Glaciology*, **32**, 102–108.

CLINE, D. W., 1997, Snow surface energy exchanges and snowmelt at a continental midlatitude Alpine site. *Water Resources Research*, **33**, 689–701.

COOPER, M. A. R., and ROBSON, S., 1996, Theory of close range photogrammetry. In *Close Range Photogrammetry and Machine Vision*, edited by K. B. Atkinson (Caithness: Whittles), pp. 9–51.

CORRIPIO, J. G., 2000, Snow surface albedo estimation using 35 mm terrestrial photography. Technical report, Kodak (Research and Development), Harrow, UK.

CORRIPIO, J. G., 2001, Snow surface albedo estimation using 35 mm terrestrial photography. *Geophysical Research Abstracts, Abstracts of the European Geophysical Society*

26th General Assembly, Nice, France, 25–30 March 2001, Vol. 3. http://www.copernicus.org/EGS/egsga/nice01/programme/abstracts/aai5922.pdf

CORRIPIO, J. G., 2003, Vectorial algebra algorithms for calculating terrain parameters from DEMs and the position of the sun for solar radiation modelling in mountainous terrain. *International Journal of Geographical Information Science*, **17**, 1–23.

CORRIPIO, J. G., and PURVES, R. S., in press, Surface energy balance of high altitude glaciers in the Central Andes: the effect of snow penitents. In *Climate and Hydrology in Mountain Areas*, edited by D. Collins, C. de Jong and R. Ranzi (London: Wiley).

CROITORU, A., and ETHROG, U., 2001, Photo orientation under unstable conditions: a robust approach using range ratios. *Photogrammetric Record*, **17**, 63–87.

DE LA CASINIÈRE, A. C., 1974, Heat exchange over a melting snow surface. *Journal of Glaciology*, **13**, 55–72.

DOZIER, J., SCHNEIDER, S. R., and MCGINNIS, D. F., 1981, Effect of grain size and snowpack water equivalence on visible and near-infrared satellite observations of snow. *Water Resources Research*, **17**, 1213–1221.

DUBAYAH, R. 1992, Estimating net solar radiation using Landsat Thematic Mapper and digital elevation data. *Water Resources Research*, **28**, 2469–2484.

FIUME, E. L., 1989, *The Mathematical Structure of Raster Graphics* (Boston: Academic Press).

FOLEY, J. D., VAN DAM, A., FEINER, S. K., and HUGHES, J. F., 1990, *Computer Graphics, Principles and Practice* (Reading, MA: Adison Wesley).

FRYER, J. G., 1996, Camera calibration. In *Close Range Photogrammetry and Machine Vision*, edited by K. B. Atkinson (Caithness: Whittles), pp. 156–180.

GREUELL, W., 2002, Validation of satellite derived surface albedos with measurements from a helicopter. *European Geophysical Society 27th General Assembly, Nice, France, 21–26 April 2002*. http://www.cosis.net/abstracts/EGS02/00689/EGS02-A-00689.pdf

GREUELL, W., and DE RUYTER DE WILDT, M., 1999, Anisotropic reflection by melting glacier ice: measurements and parameterizations in Landsat TM bands 2 and 4. *Remote Sensing of Environment*, **70**, 265–277.

GREUELL, W., KNAP, W. H., and SMEETS, P. C., 1997, Elevational changes in meteorological variables along a midlatitude glacier during summer. *Journal of Geophysical Research*, **102**, 25941–25954.

GREUELL, W., REIJMER, C. H., and OERLEMANS, J., 2002, Narrow band to broad band albedo conversion for glacier ice and snow based on aircraft and near-surface measurements. *Remote Sensing of Environment*, **82**, 48–63.

GROVER, K. D., STEVEN, M. D., RONDEAUX, G., and CLARK, J. A., 2000, Estimating albedo from limited spectral and angular data. *International Journal of Remote Sensing*, **21**, 155–165.

HOELZLE, M., and HAEBERLI, W., 1999, World Glacier Inventory. World Glacier Monitoring Service and National Snow and Ice Data Center for Glaciology, Boulder, CO. http://www-nsic.colorado.edu/NOAA/wgms inventory/

IQBAL, M., 1983, *An Introduction to Solar Radiation* (Toronto: Academic Press).

JACOBSON, R. E., 1978, *The Manual of Photography*, 7th edn (London: Focal Press).

KNAP, W. H., and REIJMER, C. H., 1998, Anisotropy of the reflected radiation field over melting glacier ice: measurements in Landsat TM bands 2 and 4. *Remote Sensing of Environment*, **65**, 93–104.

KNAP, W. H., BROCK, B. W., OERLEMANS, J., and WILLIS, I., 1999, Comparison of Landsat TM-derived and ground-based albedos of Haut Glacier d'Arolla, Switzerland. *International Journal of Remote Sensing*, **20**, 3293–3310.

KNAP, W. H., REIJMER, C. H., and OERLEMANS, J., 1999, Narrowband to broadband conversion of Landsat TM glacier albedos. *International Journal of Remote Sensing*, **20**, 2091–2110.

KODAK, 2001, Kodak technical data: Kodak professional ektachrome films E100S and E100SW. http://www.kodak.co.uk/global/en/professional/support/techPubs/e164/e164

MANNSTEIN, H., 1985, The interpretation of albedo measurements of a snowcovered slope. *Archiv für Meteorologie, Geophysik und Bioklimatologie,* **36**(Series B), 73–81.

MARKS, D., and DOZIER, J., 1992, Climate and energy exchange at the snow surface in the alpine region of the Sierra Nevada. 2. Snow cover energy balance. *Water Resources Research*, **28**, 3043–3054.

MILTON, E. J., 1989, On the suitability of Kodak neutral test cards as reflectance standards. *International Journal of Remote Sensing*, **10**, 1041–1047.

NIEMELÄ, S., RÄISÄNEN, P., and SAVIJÄRVI, H., 2001, Comparison of surface radiative flux parameterizations. Part II: Shortwave radiation. *Atmospheric Research*, **58**, 141–154.

PRATA, A. J., 1996, A new long-wave formula for estimating downward clear-sky radiation at the surface. *Quarterly Journal of the Royal Meteorological Society*, **122**, 1127–1151.

RITTER, N., and RUTH, M., 1997, The GeoTiff data interchange standard for raster geographic images. *International Journal of Remote Sensing*, **18**, 1637–1647.

RITTER, N., and RUTH, M., 2000, GeoTIFF format specification. GeoTIFF revision 1.0. http://www.remotesensing.org/geotiff/spec/geotiffhome.html

SICART, J. E., RIBSTEIN, P., WAGNON, P., and BRUNSTEIN, D., 2001, Clear-sky albedo measurements on a sloping glacier surface: a case study in the Bolivian Andes. *Journal of Geophysical Research*, **106**, 31729–31737.

SLAMA, C. C., THEURER, C., and HENRIKSEN, S. W. (editors), 1980, *Manual of Photogrammetry* (Fall Church, VA: American Society of Photogrammetry).

SPENCER, J. W., 1971, Fourier series representation of the position of the sun. *Search*, **2**, 172.

STRASSER, U., ETCHEVERS, P., and LEJEUNE, Y., 2002, Inter-comparison of two snow models with different complexity using data from an alpine site. *Nordic Hydrology*, **1**, 15–26.

TOMS–EP: 2001, Total Ozone Mapping Spectrometer—Earth Probe data sets. http://toms.gsfc.nasa.gov/eptoms/ep.html

WANG, J., ROBINSON, G. J., and WHITE, K., 2000, Generating viewsheds without using sightlines. *Photogrammetric Engineering and Remote Sensing*, **66**, 87–90.

WATT, A. H., and POLICARPO, F., 1998, *The Computer Image* (Harlow: Addison-Wesley).

WATT, A. H., and WATT, M., 1992, *Advanced Animation and Rendering Techniques: Theory and practice* (New York: Addison Wesley).

WISCOMBE, W. J., and WARREN, S. G., 1980, A model for the spectral albedo of snow, I: pure snow. *Journal of the Atmospheric Sciences*, **37**, 2712–2733.